applied sciences

MDPI

Article

Preliminary Results on Hydrogen Concentration Time Series in Spring Gases from the Pamir–Western Himalayan Syntaxis: Variability and Tectonic Instability

Jiao Tian [1,2], Jingchao Li [1,2], Yuwen Wang [1,3], Miao He [1,2], Shihan Cui [1,2], Bingyu Yao [3], Zhaojun Zeng [1,3], Jinyuan Dong [1,2], Changhui Ju [1,2], Chang Lu [1,2] and Xiaocheng Zhou [1,2,*]

[1] United Laboratory of High-Pressure Physics and Earthquake Science, Institute of Earthquake Forecasting CEA, Beijing 100036, China; tianjiao375@163.com (J.T.); lijc@ief.ac.cn (J.L.); wyw20010122@163.com (Y.W.); hemiao@ief.ac.cn (M.H.); c1416102468@163.com (S.C.); zzj00616@163.com (Z.Z.); dongjinyuan@163.com (J.D.); juchanghui15@mails.ucas.ac.cn (C.J.); cealuchang@163.com (C.L.)
[2] Key Laboratory of Earthquake Forecasting and Risk Assessment, Ministry of Emergency Management, Beijing 100036, China
[3] School of Earth Sciences and Resources, China University of Geosciences, Beijing 100083, China; yaobingyu2022@163.com
* Correspondence: zhouxiaocheng188@163.com

Abstract

Identifying reliable geochemical signals that reflect crustal stress evolution remains a major challenge in earthquake monitoring. Spring fluids, due to their deep circulation and rapid response, provide an important window into fault-zone processes. This study presents three years (May 2022–March 2025) of hourly hydrogen gas (H_2) concentration monitoring in spring gases from the Muji Basin on the northern Pamir Plateau, integrated with meteorological and seismic data. H_2 concentrations exhibited a stable diurnal pattern, positively correlated with water and air temperatures and negatively correlated with atmospheric pressure. Short-term anomalies during seismically quiet periods may reflect a combination of temperature-dependent solubility effects and transient degassing caused by localized gas accumulation and sudden release under heterogeneous fault and aquifer conditions. During seismically active phases, sustained increases in H_2 concentrations were also recorded; however, such anomalies did not consistently precede earthquakes, instead reflecting broader phases of tectonic instability and episodic fault-zone degassing. These findings highlight the potential of long-term H_2 monitoring to improve our understanding of the coupling between crustal stress, fluid transport, and degassing processes in tectonically active regions.

Keywords: spring water; hydrogen gas; time series; earthquake; Pamir Plateau

check for updates

Academic Editor: Nicholas Vassiliou Sarlis

Received: 30 July 2025
Revised: 27 August 2025
Accepted: 3 September 2025
Published: 4 September 2025

Citation: Tian, J.; Li, J.; Wang, Y.; He, M.; Cui, S.; Yao, B.; Zeng, Z.; Dong, J.; Ju, C.; Lu, C.; et al. Preliminary Results on Hydrogen Concentration Time Series in Spring Gases from the Pamir–Western Himalayan Syntaxis: Variability and Tectonic Instability. *Appl. Sci.* **2025**, *15*, 9736. https://doi.org/10.3390/app15179736

1. Introduction

Earthquake prediction remains one of the most challenging scientific problems globally. The question "Are there reliable precursors that could help predict earthquakes?" has been recognized as one of the 125 most important unanswered scientific questions [1]. Seismologists have long sought sensitive and reliable natural precursor signals, aiming to detect anomaly patterns and understand the underlying mechanisms that may help forecast the time, location, and magnitude of future earthquakes [2,3].

Among various approaches, fluid geochemistry has emerged as a promising tool for detecting earthquake precursors. During earthquake preparation and occurrence,

changes in crustal stress can modify rock porosity, thereby influencing fluid migration pathways [4,5] and storage conditions [6,7]. These physical changes alter the chemical and isotopic composition of subsurface fluids [8–10]. On the basis of this principle, researchers have conducted continuous surface monitoring to detect temporal changes in geochemical indicators and evaluate fluid responses to seismic processes. Prior studies have mainly focused on groundwater chemical and dissolved gases in wells [11–13], as well as soil gases along fault zones, including Rn, CO_2, CH_4, and H_2 [14–17]. These efforts have yielded large datasets and identified numerous earthquake-related anomalies. Recently, with advancements in real-time chemical monitoring, hot spring fluids, representing deep-circulating groundwater, have demonstrated unique advantages. Compared with shallow groundwater, hot spring water circulates deeper and flows more rapidly [18–20]. In contrast to soil gases, dissolved gases in bubbling springs are derived from greater depths and are less affected by atmospheric contamination [21–23]. Consequently, chemical and isotopic changes in spring fluids can provide more timely, accurate, and profound insights into subsurface geological processes.

H_2 can be generated during tectonic activity along fault zones [24–26]. This process results from both chemical and mechanical transformations in rocks. During fault slip, rock fracturing and pulverization expose fresh mineral surfaces with high chemical reactivity. One hydrogen-generating mechanism involves the hydrolysis of Si and Si–O radicals, which are produced when Si–O–Si bonds between SiO_4 tetrahedra in silicate minerals are broken under deep crustal conditions [27]. Additionally, hydrogen may be released from hydroxyl groups embedded within mineral lattice under high-temperature and high-pressure conditions. In such environments, hydroxyl pairs (e.g., O_3Si–OH) may dissociate to release hydrogen [28]. These fault-related hydrogen-producing reactions have been documented during earthquakes in Japan and the United States [29–31]. In China, elevated H_2 concentrations in hydrothermal systems were observed along the Longmenshan Fault following the 2008 Wenchuan *M* 8.0 earthquake [32]. Therefore, changes in H_2 concentrations have been widely regarded as a critical and non-negligible indicator in gas monitoring related to fault activity and seismic assessment [33,34].

Recent developments in the real-time monitoring of H_2 dissolved in spring water have further highlighted its relevance to seismic activity. These systems have revealed promising correlations between H_2 concentration changes and earthquakes, including distinct pre-seismic anomalies. As a result, there has been growing interest in long-term hydrogen monitoring in hydrothermal settings. For instance, Zhou et al. [35] implemented continuous gas monitoring at a hot spring along the Zemuhe Fault on the eastern margin of the Tibetan Plateau. Their results showed that precursor anomalies in H_2 concentrations emerged 5 to 60 h before natural earthquakes, whereas only post-seismic responses were observed for anthropogenic events. Nevertheless, several key questions remain: how do hydrothermal H_2 concentrations evolve over extended periods? What controls these variations? And how does H_2 respond to different seismic processes? These questions warrant further investigation.

This study presents three years of the continuous hourly monitoring of dissolved H_2 concentrations at a bubbling spring in the Muji Basin, located within the Western Himalayan Syntaxis. Environmental parameters, including water temperature, air temperature, and atmospheric pressure, were recorded simultaneously. Additionally, daily precipitation data and earthquake catalog records were collected. On the basis of this comprehensive dataset, the temporal patterns of H_2 release and their coupling with environmental factors were analyzed. The responses of dissolved H_2 concentration to seismic events were also assessed, and the potential influencing factors were discussed. This work aims to enhance our understanding of the relationship between variations in spring gas concentrations and

seismic activity and to provide scientific support for earthquake assessment relying on real-time gas monitoring.

2. Geological Settings

The Pamir–Western Himalayan Syntaxis marks the western terminus of the Indo-Asian collision zone (Figure 1a). This syntaxis is bounded to the north by the Main Pamir Thrust and to the south by the Main Boundary Thrust and Main Frontal Thrust [36]. The eastern boundary is defined by the approximately 1000 km long right-lateral Karakoram fault, which extends from eastern Pamir to southwestern Tibet [37,38]. Tectonic studies, including GPS velocity fields and focal mechanism solutions, indicate intense compressional shortening along the northern and western edges of Pamir (Figure 1b) [39]. In contrast, central and western Pamir are separated from eastern Pamir by the 205 km long Kongur Shan extensional system, which accommodated east–west extension in northern Pamir, together with Karakul Rift in central–northern Pamir [40,41].

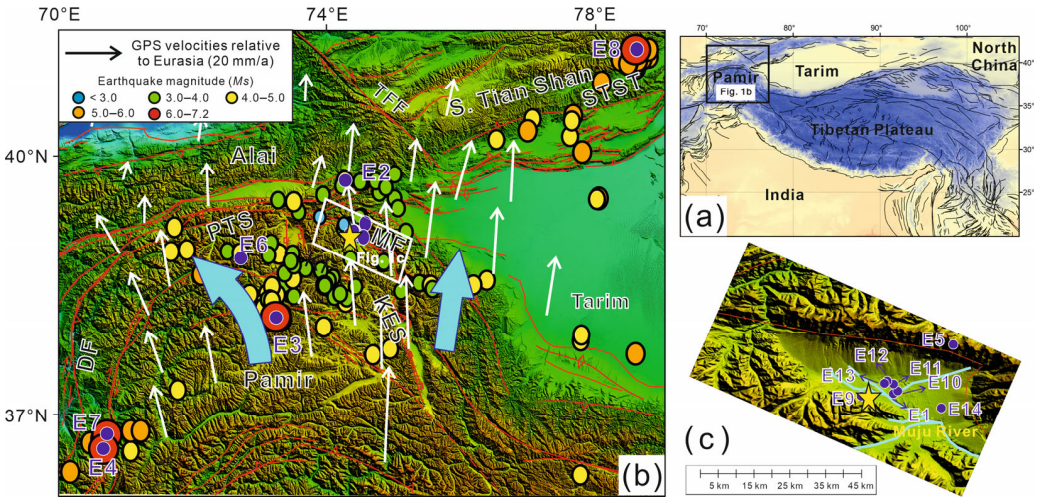

Figure 1. (**a**) Regional tectonic map of the Pamirs and Tibetan regions. (**b**) Major fault structures in Pamir, with movement shown by blue arrows from GPS velocities [41]. Yellow star marks the spring monitoring station (39.083° N, 74.328° E). Purple dots represent earthquakes selected by the magnitude algorithm in Section 3.3, identified as likely showing precursor anomalies at the observation station. Blue, green, yellow, orange, and red dots represent earthquakes of varying magnitudes, selected using the seismic energy density algorithm (with energy densities > 10^{-5} J/m^3). Details in Table S1; (**c**) enlarged topographic map of the Muji Basin, highlighting the observation station and the locations of selected earthquakes. DF = Darvaz Fault, KES = Kongur Extensional System, MF = Muji Fault, PTS = Pamir Thrust System, STST = Southern Tian Shan Thrust, TFF = Talas–Fergana Fault.

The Muji Fault is a 60 km long, south–southwest-dipping structure located at the northern end of the Kongur Shan extensional system. It trends northwest–west and intersects the Kongur Shan fault system to the east, while potentially connecting with the Pamir reverse fault system to the west. The fault displays a change in kinematics, transitioning from right-lateral strike-slip motion in the west to normal faulting in the east. At its eastern terminus, the fault changes strike from west–northwest to north, where it transitions into the Kongur Shan normal fault [42,43]. The Muji Fault delineates the boundary between rugged, glacier-covered mountains to the north and the Muji Basin, a graben formed by faulting along the Muji Fault and Kongur Extensional System, to the south. According to high-resolution satellite imagery and GPS topographic measurement, the Muji Fault exhibits a horizontal slip rate of 11.5 ± 2.3 mm/a and a vertical offset of 105 ± 12 m since approximately 16.8 ± 3.5 ka [44].

The Muji Basin is an active, triangular-shaped tectonic basin controlled by late Neogene to Quaternary faulting (Figure 1c). It is characterized by higher elevations in the northwest and lower elevations in the southeast and is subjected to a north–south compressive stress field due to its proximity to the Pamir Plateau [45,46]. The exposed stratigraphic in the basin includes the Mesoproterozoic Blenquolle Group, Silurian, Devonian Kiziltau Formation, Lower Permian, and Cenozoic lacustrine and alluvial deposits. The Blenquolle Group, a regional metamorphic sequence, crops out the Muji–Bulunkuo–Tashkurgan–Azgar area and comprises lower biotite–plagioclase gneiss, granitic gneiss, marble, and biotite schist and quartzite. This sequence also contains strata from the Neoproterozoic, Early Paleozoic, and Permian. The Silurian units consist of muscovite–quartz schist, biotite granite gneiss, and marble. The Kiziltau Formation represents a shallow marine sedimentary sequence mainly composed of conglomerates, sandstones, and limestones. Lower Permian rocks are mainly conglomerates, sandstones, marbles, tuff, and limestones. The Cenozoic succession is dominated by Upper Pleistocene alluvial and glacial deposits, including gravel layers, Holocene alluvial gravel, and lacustrine fine sand and silt layers [47].

The Muji Basin experiences a plateau mountain climate, with an average annual temperature of 0.7 °C. January temperatures average −12.5 °C, while July temperatures reach approximately 11 °C. The region lacks pronounced seasonal variation and is generally divided into cold and warm periods. Annual precipitation ranges from 80 to 200 mm, mostly occurring in summer. From November to April, the climate is cold and dry with minimal snowfall, whereas from May to October, temperatures rise and precipitation increases. The main hydrological system is composed of the Muji River and its tributaries, which originate from the southern slopes of the Kungai Mountains to the north and the northern slopes of the Sarekule Mountains to the south. These rivers are fed by glacier meltwater, springs, and atmospheric precipitation, ultimately discharging into the Gaizi River [47].

3. Data Acquisition and Processing Methods

3.1. Data Acquisition

The main components of the online monitoring system for hydrogen concentration in spring gases are shown in Figure 2. A custom-made polytetrafluoroethylene gas collection funnel is inverted and positioned over the spring outlet to capture gas emissions. The funnel outlet is connected to a high-efficiency water–gas separator via a flexible hose, which subsequently connects to the inlet of a trace hydrogen online analyzer. This analyzer is equipped with temperature and pressure sensors, allowing for the hourly recording of ambient temperature and atmospheric pressure. A water temperature probe is installed above the funnel. The entire system is powered by solar energy, and data transmission is achieved via 4G wireless communication. The trace hydrogen analyzer has a measurement range of 0–5000 ppm, a detection limit of $\leq$0.005 ppm, and an average relative standard deviation (RSD) of $\leq$5%. The water temperature probe operates within a range of 0–100 °C, with a resolution of 0.06 °C and an accuracy of 0.3 °C. Both hydrogen concentration and water temperature are measured on an hourly basis.

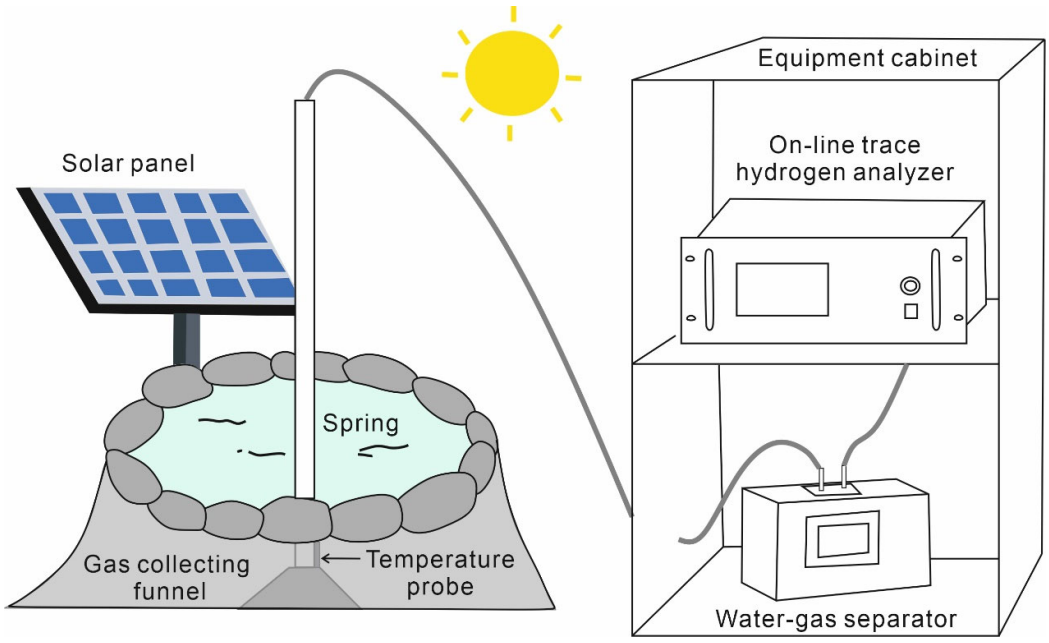

Figure 2. Schematic diagram of hydrogen concentration monitoring system.

Additionally, the earthquake catalog used in this study was obtained from the China Earthquake Networks Centre. The catalog provides detailed information on earthquake locations, magnitudes, and focal depths, covering the period from May 18, 2022 to March 4, 2025, and includes all events with magnitudes of *Ms* 1.0 and above. Daily rainfall data were acquired from the nearest meteorological station, located in the Kizilsu Kirghiz Autonomous Prefecture, approximately 154 km from the monitored spring. These data were downloaded from the National Meteorological Information Center.

3.2. Missing Data and Handling Approaches

Using the observation methods described above, hourly data for H_2 concentration and water temperature were collected from 00:00 on 18 May 2022 to 23:00 on 4 March 2025, covering a total period of 1022 days. A total of 24,528 data points were recorded for each parameter: H_2 concentration, water temperature, air pressure, and air temperature (Table S1). However, due to equipment malfunctions, power outages, and other external factors, some data points are missing. Specifically, 4089 H_2 concentration values, 4636 water temperature values, 4143 air pressure values, and 4143 air temperature values were missing, corresponding to missing data rates of 16.67%, 18.90%, 16.85%, and 16.85%, respectively.

Handling missing values in time series data is a critical preprocessing step, as appropriate treatment improves the accuracy and stability of subsequent models. Given the strong daily and annual cycles observed in the data, a seasonal decomposition interpolation method [48,49] was employed to impute the missing values. This method can use either an additive or multiplicative model. Since the amplitude of seasonal variations in this dataset remains relatively constant, the additive model was selected.

The seasonal decomposition interpolation method decomposes a time series (Y) into three components, trend (T), seasonal (S), and residual components (I), with the relationship expressed as follows:

$$Y = T + S + I \quad (1)$$

Missing values are imputed by processing each component individually and then recombining them to reconstruct the full series. This method effectively captures distinct

seasonal and daily patterns, resulting in more accurate imputation. The specific steps are as follows:

1. Decompose the time series: The time series breaks down into trend, seasonal, and residual components using the additive model.
2. Missing value imputation:

- The trend component is interpolated by means of linear interpolation.
- The seasonal component is imputed by applying the forward fill method, where each missing value is replaced by the most recent non-missing value. For consecutive missing values, the same preceding value is used until a new non-missing value appears.
- The residual component is imputed by utilizing the mean of the available values.

3. Reconstruct the series: The interpolated trend, seasonal, and residual components are summed to generate the final imputed time series.

All data processing was conducted by using Python 3.13.3, with relevant libraries including pandas, numpy, and statsmodels.

3.3. Earthquake Catalog Selection

3.3.1. Influence Radius as a Selection Criterion

During earthquake preparation, tectonic stresses create a zone of fractured rock in the focal region. This zone can be modeled as a solid inclusion with altered mechanical properties, leading to stress redistribution and surface deformations [50,51]. The influencing radius (ρ, km) defines the extent of deformation and the area where earthquake precursors may appear.

The influence radius is calculated by means of the following formula:

$$\rho = 10^{0.43M} \quad (2)$$

where M is the earthquake magnitude [52]. Derived from the theory of soft elastic inclusion in an elastic half-space, this equation estimates deformation and tilt at the Earth's surface using earthquake magnitude and epicentral distance. The influence radius delineates the region in which precursor phenomena, such as changes in physical and chemical properties, are likely to occur. For reference, the influence radii for earthquakes of magnitude 1 to 8 are approximately 3, 7, 20, 53, 141, 380, 1023, and 2754 km, respectively.

3.3.2. Seismic Energy Density as a Selection Criterion

Seismic energy density quantifies the intensity of energy released by an earthquake and is influenced by both the earthquake magnitude and the distance from the epicenter. It is defined by the amplitude of seismic waves and the extent of energy propagation [53]. Seismic energy density increases with earthquake magnitude and decreases with distance.

$$l\log \mathrm{e} = 1.45M - 3.19 - 3.04\, l\log \mathrm{r} \quad (3)$$

where e is the seismic energy density (in $\mathrm{J/m^3}$), M is the magnitude, and r is the distance from the observation point to the epicenter (in km). Higher values of e indicate stronger energy release and potentially greater impact.

4. Results

4.1. General Overview of the Data Distribution

Table 1 summarizes the descriptive statistics of the observed time series. The H_2 concentrations ranged from a minimum of 0.11 ppm to a maximum of 33.65 ppm, with a median of 0.47 ppm and a mean of 0.82 ppm. The ranges for water temperature, air temperature,

and atmospheric pressure were 6.06–10.63 °C, –26.64–40.54 °C, and 645.60–674.95 mmHg, respectively. The median values were 8 °C (water temperature), 6.87 °C (air temperature), and 664.96 mmHg (atmospheric pressure), while the corresponding means were 8.12 °C, 7.05 °C, and 664.56 mmHg. The close alignment between the median and mean values for water temperature and atmospheric pressure indicates relatively symmetric distributions. In contrast, the noticeable deviations in air temperature and H_2 concentration suggest skewed distributions. The modes varied across the datasets, with their relationships to other central tendency measures reflecting the unique characteristics of each distribution. The distribution shapes also varied across parameters. Atmospheric pressure showed positive kurtosis, indicating a left-skewed distribution. Air temperature exhibited slightly lower kurtosis than a normal distribution, with mild left skew. Water temperature's kurtosis was close to that of a normal distribution, but slightly right-skewed. In contrast, the H_2 concentration displayed high kurtosis and strong right skew, reflecting its heavy-tailed distribution. These differences suggest distinct underlying mechanisms: air temperature, influenced by complex meteorological factors, exhibits a broader and flatter distribution, whereas H_2 concentration, shaped by geological or chemical processes, is more peaked and asymmetric. To enable a more intuitive comparison of variations across measurement items, the coefficient of variation (CV = standard deviation/mean × 100%), which is dimensionless and unaffected by unit conversion, is relied upon. Air temperature exhibits the largest relative variability (CV = 187.85%), followed by H_2 concentration (CV = 143.96%). Both indicate strong temporal fluctuations compared to their mean values. By contrast, water temperature shows moderate variability (CV = 8.90%), while atmospheric pressure remains extremely stable (CV = 0.59%). These results highlight that H_2 concentrations and air temperature are the most dynamic components in the monitoring system, whereas water temperature and especially air pressure show much lower relative variability.

Table 1. Descriptive statistics of H_2 concentration (H_2 Con., ppm), water temperature (WT, °C), air temperature (AT, °C), and air pressure (AP, mmHg). Except for the coefficient of variation, kurtosis, and skewness (which are dimensionless), all other statistical metrics retain the same unit as the original data.

Variable	H_2 Con.	WT	AT	AP
Mean	0.82	8.12	7.05	664.56
Standard error	0.01	0.01	0.09	0.03
Median	0.47	8.00	6.87	664.96
Mode	0.14	7.88	17.88	665.71
Standard deviation	1.19	0.72	13.25	3.96
Coefficient of variation	143.96%	8.90%	187.85%	0.59%
Variance	1.41	0.52	175.46	15.69
Kurtosis	104.27	−0.16	−0.89	0.81
Skewness	7.04	0.51	0.03	−0.62
Minimum	0.11	6.06	−26.64	645.60
Maximum	33.65	10.63	40.54	674.95

According to the violin plots shown in Figure 3, the distribution characteristics of the data for the four measured parameters are as follows: For H_2 concentration, the median is low, and the whiskers are short, indicating a tendency toward smaller values with most of the data concentrated in the lower range. For water temperature, the median is centered, and the whiskers are long, with more data concentrated in the lower-value region. For air temperature, the median is slightly below the center, and the whiskers are long, with a relatively even distribution across the range. For air pressure, the median is high, the whiskers are short, and the distribution is compact, with most of the data concentrated in the higher-value region.

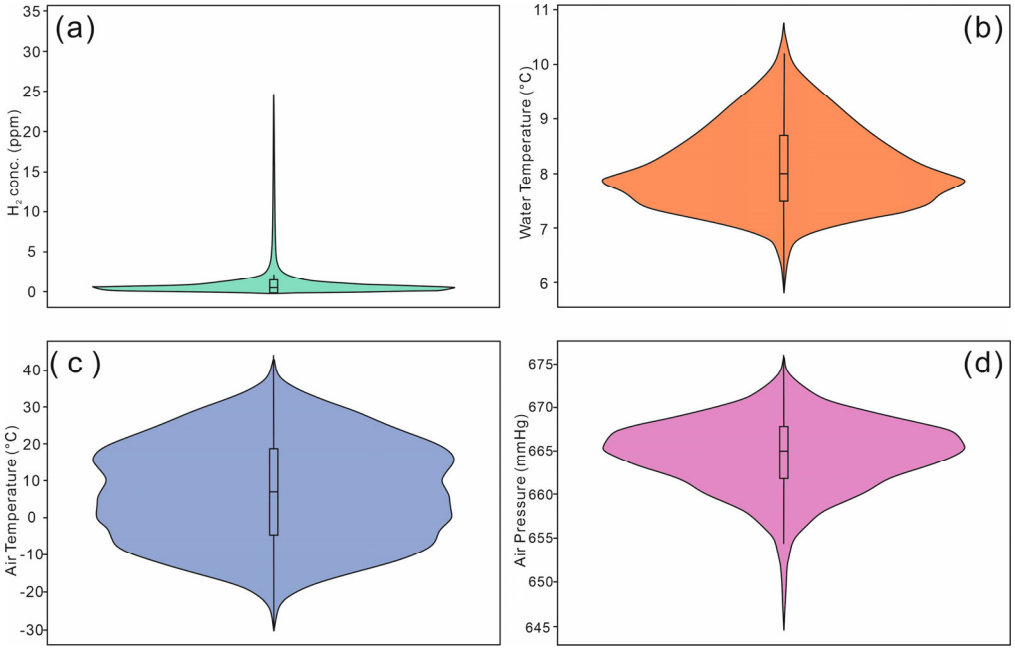

Figure 3. Violin plots showing the distribution of data for different variables: (**a**) H_2 concentration, (**b**) water temperature, (**c**) air temperature, and (**d**) air pressure. The shape of each violin plot is determined using kernel density estimation. The box part of each plot is bounded by the upper and lower quartiles, with the central horizontal line representing the median. The whiskers extend from the edges of the box to 1.5 times the interquartile range, capturing potential outliers.

During the 1022-day observation period, rainfall was recorded on 105 days, with the maximum daily rainfall reaching 11.94 mm. As shown in Supplementary Figure S1, precipitation was concentrated during the warmer months (May to October), while rainfall in the colder months was minimal, except for an isolated event on 13 January 2023, when 8.38 mm was recorded. Although a clear seasonal pattern was evident, no consistent annual or seasonal periodicity in rainfall was observed.

On the basis of the two earthquake catalog selection criteria described earlier, the results are as follows: As listed in Supplementary Table S1, a total of 14 earthquakes were identified within their respective influence radii, with magnitudes ranging from *Ms* 2.0 to 7.2, focal depths of 5–230 km, epicentral distances of 2–440 km, and seismic energy densities between 4.36×10^{-4} and 3.1 J/m^3. The results from the second method, using seismic energy density, yielded 143 qualifying earthquakes with values exceeding 1×10^{-5} J/m^3 at the observation site (Supplementary Table S1). These events had a focal depth of 1–280 km, magnitudes of *Ms* 1.1–7.2, and epicentral distances of 2–560 km, with corresponding seismic energy densities ranging from 1×10^{-5} to 3.1 J/m^3. It should be noted that the 14 earthquakes identified by applying Dobrovolsky's criterion were included within this broader set. These events primarily reflect variations in seismic energy influence over time. As shown in Figure 1b, small to moderate-magnitude earthquakes are concentrated near the KES, whereas the stronger events affecting the observation site mainly occurred along the STST to the northeast and the DF to the southwest. These patterns indicate intense tectonic activity in these regions, with energy transmission pathways directly or indirectly linked to the geological structures of the Muji Basin.

4.2. Variation Characteristics of the Observed Time Series

To examine variations in the monitored parameters, observation curves were plotted for each variable over both 24 h cycles and the full monitoring period, as shown in Figure 4. It is important to note that the use of seasonal interpolation did not distort the overall

trends or introduce artificial anomalies. While all parameters exhibited clear diurnal cycles, their long-term patterns lacked consistent regularity. The detailed analysis is as follows:

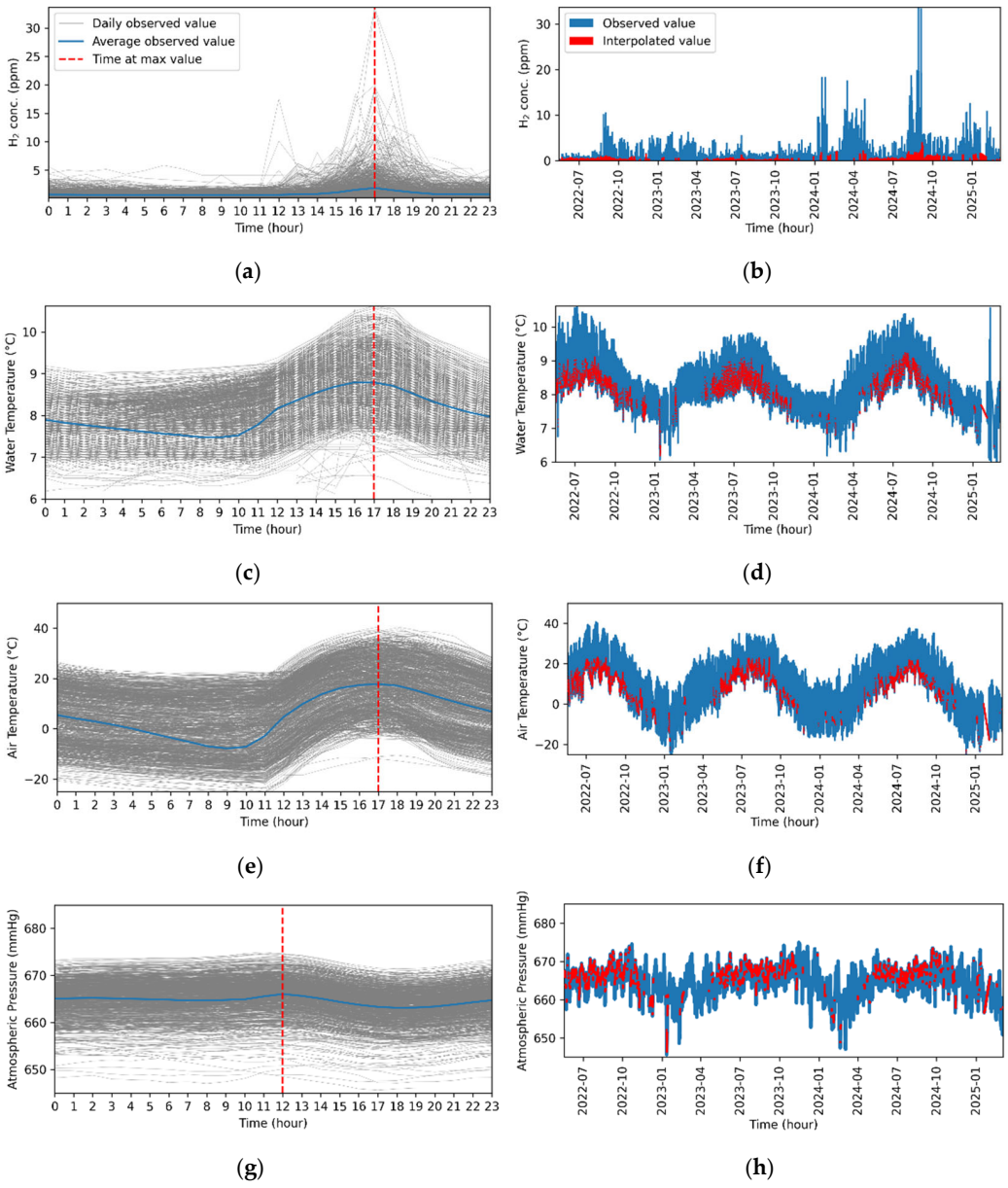

Figure 4. (**a**,**c**,**e**,**g**) show the 24 h variation curves of H_2 concentration, spring water temperature, air temperature, and atmospheric pressure, respectively. The gray lines indicate daily fluctuations, the blue lines represent the average of valid data, and the red dashed lines highlight the times corresponding to the daily peaks. (**b**,**d**,**f**,**h**) display the hourly variations in these parameters over the entire observation period, with the blue lines representing actual observations and the red lines showing values interpolated using a seasonal method.

As illustrated in Figure 4a, H_2 concentrations display a reproducible diurnal cycle, with elevated levels consistently occurring between 12:00 and 19:00, and markedly lower levels from 19:00 through to 11:00 the next day, during which concentrations rarely exceeded 5 ppm. This stable temporal pattern supports the reliability of the measurements and suggests that the observed H_2 increases are due to genuine geogenic emissions rather than instrumental errors or environmental interference. Similarly, water and air temperatures follow regular daily cycles. The diurnal fluctuations in water (Figure 4c) and air temperatures (Figure 4e) resemble a cosine wave, with minimum values typically around

10:00 and 23:00, and peaks around 17:00, coinciding with the peak H_2 concentration. In contrast, atmospheric pressure (Figure 4g) follows a sine wave-like pattern with smaller amplitude, peaking around 12:00 and reaching its minimum near 17:00.

Over the entire monitoring period (Figure 4b), several distinct short-term spikes in H_2 concentration were observed, but they lacked any consistent or periodic pattern. Notably, as shown in the diurnal variation in Figure 4a, these elevated H_2 episodes did not result in sustained high concentrations. Instead, the daily pattern persisted, with elevated values confined to the 12:00–19:00 window and values remaining below 5 ppm at other times. Regarding long-term trends, water (Figure 4d) and air (Figure 4f) temperatures exhibit synchronized seasonal cycles, with peaks during July and August and troughs around January. Atmospheric pressure followed a similar seasonal trend (Figure 4h), with higher values typically observed in October and lower values from February to March. These annual variations in air temperature and atmospheric pressure reflect the characteristics of the subtropical monsoon climate prevalent in Central Asia.

5. Discussion

5.1. Correlation Between H_2 Concentration and Meteorological Factors

To analyze the periodicity of the datasets, periodograms were computed using Fast Fourier Transformation (FFT). Specifically, for a time series x_t of length n, the FFT was applied to compute X(f), and the power was estimated as $|X(f)|^2/n$. Only positive frequencies were retained, and periods were expressed in hours. Overall, the FFT periodograms of H_2 concentration (Figure 5a), water temperature (Figure 5b), air temperature (Figure 5c), and air pressure (Figure 5d) exhibit prominent peaks at 12 and 24 h, consistent with the diurnal variations observed in Figure 4. This clearly indicates two dominant harmonic modes, 12 h and 24 h cycles, present across all parameters. These periodic patterns suggest that the diurnal variations in the H_2 concentration are primarily driven by corresponding fluctuations in meteorological factors such as water temperature, air temperature, and air pressure. This phenomenon aligns with thermodynamic principles and is commonly observed in atmospheric processes governed by solar radiation. During daylight hours, increased solar radiation raises air and water temperatures, and according to the ideal gas law [54], this results in a decrease in air pressure. Concurrently, temperature influences the solubility of gases in water: as temperatures rise, gas solubility decreases, leading to greater degassing. Around 17:00, when both air and water temperatures peak, the solubility of H_2 in water drops significantly, and a larger amount escapes into the atmosphere, causing concentration levels to reach a maximum in accordance with Henry's Law [55]. Conversely, in the early morning and evening, radiative cooling and the absence of solar input led to decreased temperatures around 10:00 and 23:00. In addition, the FFT periodograms of water temperature, air temperature, and air pressure reveal another significant peak at approximately 8760 h, corresponding to the annual cycle of 365 days, which reflects seasonal variability. The H_2 concentrations, however, do not exhibit a strong peak at this frequency. Instead, they display multiple pronounced periodicities, suggesting that other natural or geological factors, operating on different timescales, may also influence H_2 variability. It should be clarified that the periodograms were computed as the squared modulus of the discrete Fourier transform of the time series was obtained, and no further smoothing, averaging, or windowing was applied; thus, the results represent raw spectral power estimates. Although such estimates are known to be biased and inconsistent as formal estimators of the power spectrum [56], they are sufficient to reveal the dominant diurnal cycles (12 h and 24 h) in this study.

The FFT periodogram of rainfall (Figure 5e), by contrast, exhibits irregular fluctuations without dominant or stable periodic peaks. At shorter periods (between 0.1 and 1 h),

power values show dense, low-amplitude oscillations lacking a clear periodic structure. Although a relatively higher peak is observed near 10^1 h, it is isolated and unsupported by adjacent periodicities, indicating that precipitation does not display clear periodic behavior or synchronous variation with other meteorological factors or H_2 concentrations.

To assess the linear relationships, Pearson correlation coefficients were calculated between the H_2 concentration and various meteorological parameters. As shown in Supplementary Figure S2, the absolute correlation coefficients are generally low. The H_2 concentration shows a weak positive correlation with water and air temperatures and a weak negative correlation with air pressure and precipitation. However, all linear relationships are minimal, making it difficult to explain or predict H_2 concentrations by relying solely on these variables. Consequently, there is no need to apply data corrections to remove meteorological influences from the H_2 dataset. It should also be noted that the precipitation data were originally recorded on a daily basis. To match the hourly resolution of other measurements, daily precipitation values were evenly divided across 24 h, an approximation that assumes uniform distribution, which may not reflect actual rainfall patterns. Furthermore, the precipitation data were obtained from a meteorological station approximately 145 km from the geothermal observation site, which may reduce the reliability of the correlation analysis between the H_2 concentration and precipitation.

In summary, while meteorological factors strongly influence the diurnal variation in H_2 degassing in geothermal springs, they cannot fully explain the irregular and large-scale fluctuations, spanning three orders of magnitude, observed over the 1022-day monitoring period. This implies that tectonic processes, such as earthquakes, may play a critical role in modulating H_2 emissions.

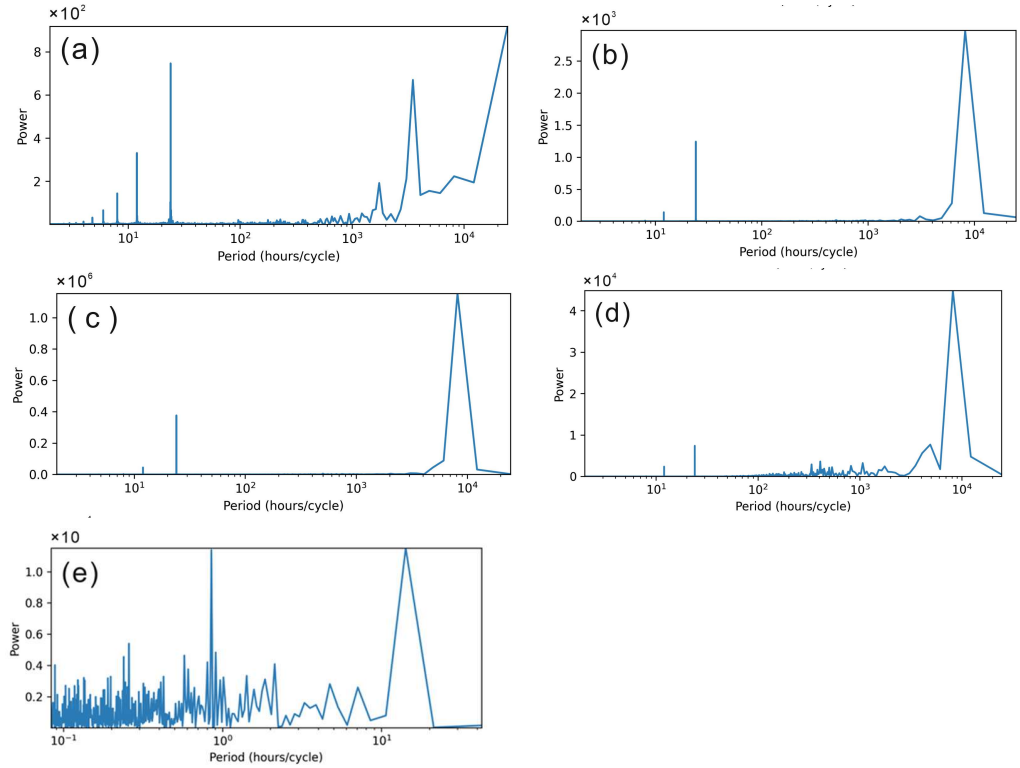

Figure 5. FFT periodogram of (**a**) H_2 concentrations, (**b**) water temperature, (**c**) air temperature, (**d**) air pressure, and (**e**) precipitation.

5.2. Correlation Between H_2 Concentration and Seismic Activities

5.2.1. Anomaly Detection in H_2 Concentration

The large CV of H_2 indicates its high sensitivity to external perturbations, whereas the low CVs of water temperature and atmospheric pressure reflect their buffering capacity and limited direct response to short-term tectonic processes. Building on this contrast, we next investigate the relationship between H_2 concentration and a typical indicator of crustal instability—earthquake activity. While the previous section examined the regular variations in the H_2 concentration and their correlation with meteorological factors, detecting anomalous changes in the data is a necessary prerequisite for identifying variations potentially associated with seismic events. Therefore, it is essential to analyze anomalies in the H_2 concentration time series before exploring its relationship with seismic activity.

Time series data often contain multiple components, including long-term trends, cyclical patterns, seasonal fluctuations, and irregular variations. To isolate these components and minimize the influence of regular factors such as meteorological conditions, decomposition techniques are commonly applied. These include seasonal trend decomposition [48,49] and empirical mode decomposition [57]. For anomaly detection, a variety of data processing methods have been employed, such as multiple linear regression [57], singular spectrum analysis [58], machine learning techniques [59,60], wavelet power spectrum analysis [10], boxplot analysis [61], and moving average methods [62–64]. Some studies integrate multiple approaches to enhance detection accuracy [65,66]. The primary goal of these methods is to identify both regular and anomalous data changes, enabling the isolation of anomaly components for further analysis, especially in relation to seismic events [10,59,61,65]. However, the aforementioned techniques are most effective for continuous observational datasets where distinguishing between anomalies and background values is subtle and challenging. In cases where anomalies and background values differ significantly, simple data processing methods can yield more accurate anomaly detection results. For instance, some studies define anomaly thresholds using standard deviation multiples, such as two standard deviations [62,63,66] or three standard deviations [67]. Alternatively, fluctuations in observational data can be directly compared with seismic events [68].

In this study, the H_2 concentration time series (Supplementary Figure S3) reveals that although the maximum value reaches 33.65 ppm, most observations fall within a lower concentration range, with fewer high-concentration values. The lower quartile is 0.26 ppm, and the upper quartile is 0.90 ppm. Notably, 90.36% of the values are below 1.62 ppm, 95.29% are below 2.48 ppm, and 96.54% are below 2.98 ppm, which correspond to the mean plus two standard deviations. The analysis of previous observations (Figure 4b) shows no significant trends or periodic variations related to meteorological factors, indicating a stable background with clearly distinguishable outliers. To address this, we applied the residual signal processing technique proposed by Fu et al. [63,69] to suppress regular fluctuations and detect anomalies potentially associated with seismic activities. This method was later adopted by Barkat et al. [62] to detect seismic anomalies in soil radon data in Northern Pakistan, yielding promising results. This technique compares the daily average of hourly observations (also known as the trend line) with a rolling average over a 7-day or 14-day window. In this study, a 7-day rolling average was applied to compute the moving average. The residual concentration, denoted as d$A(t)$, is calculated as the difference between the daily average A(t) and the rolling average R$A(t)$, as expressed in the following equation:

$$dA(t) = A(t) - \mathrm{R}A(t) \quad (4)$$

Anomalies in the residual concentration are identified by the use of a statistical threshold defined as the mean ± two standard deviations ($\bar{x} \pm 2\sigma$), which correspond to a 95% confidence interval [62,70].

As shown in Figure 6a, the raw hydrogen concentration values (blue bars) exhibit substantial fluctuations. The daily average (purple line) is relatively stable, though minor variations persist. The 7-day rolling average (orange dashed line) further smooths the data, revealing a stable overall trend. The threshold defined by the raw mean plus two standard deviations (Meanraw + 2 * Std; blue horizontal line) serves as a reference. During certain periods, peak hydrogen concentrations exceed this threshold (2.98 ppm), indicating significant anomalous fluctuations. The residual hydrogen concentration values serve as a filtering tool, highlighting detailed changes after removing short-term trends. This enhances the amplitude of signal peaks and improves the identification of intervals exceeding the anomaly threshold ($\bar{x} \pm 2\sigma$) (Figure 6b). It was observed that positive anomalies in the residual hydrogen concentration were frequently accompanied by negative anomalies of a similar magnitude. This pattern likely reflects an artifact of the algorithm rather than actual decreases in the hydrogen concentration, since the baseline remains stable and only positive peaks are evident in the daily average curve (Figure 6a). Therefore, in Figure 6b, consecutive positive and negative anomalies are interpreted as part of the same anomaly group.

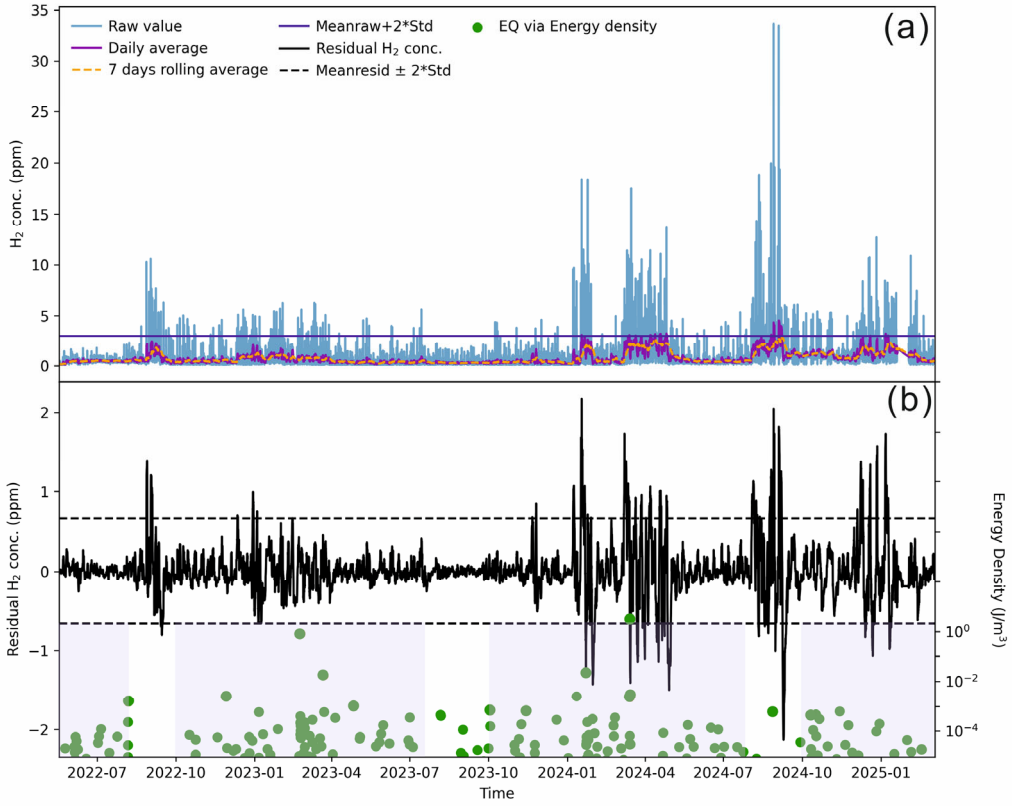

Figure 6. (**a**) Temporal variation in raw H_2 concentration, shown with 24 h and 7-day rolling averages; "Meanraw+2 * Std" indicates the mean plus two standard deviations (2.98 ppm). (**b**) Residual H_2 concentration calculated using Eq. (4), with thresholds defined by $\bar{x} \pm 2\sigma$; "Meanresid ± 2 * Std" represents the mean ± two standard deviations. The scatter plot (green dots) displays seismic events with energy density > 10^{-5} J/m^3 at the observation point. Purple shaded areas mark time intervals of intensive seismic activity.

5.2.2. H_2 Anomalies and Seismic Activity as Tectonic Instability Indicators

As is well known, seismic activity is a product of tectonic processes, and the level of seismic activity serves as an indicator of tectonic dynamics [71]. To investigate the relationship between H_2 release and tectonic activity, seismic events are plotted in Figure 6b as a scatter plot representing energy density at the observation site. It is important to note that the use of seismic energy density as a composite parameter is grounded in the following rationale: though previous studies have often relied solely on earthquake magnitude [20,62,72,73] or individual events [12,74,75] to correlate with geochemical anomalies, magnitude alone does not adequately reflect the true seismic impact at the monitoring site. Variables such as epicentral distance, focal depth, fault geometry, and source mechanism all play critical roles. While there is no unified physical parameter that can integrate these factors, the post-seismic energy density method employed in this study considers both magnitude and distance, offering a more objective basis for identifying seismic events related to hydrogen anomalies. Thus, seismic events where the post-seismic energy density at the observation site exceeds 1×10^{-5} J/m^3 (a value lower than the minimum energy density of 10^{-4} J/m^3 for spring water responses to earthquakes, as reported by Tian et al. [18]) are marked as green dots in the scatter plot.

Regarding the frequency of seismic events (Figure 6), four seismic clusters were observed during the monitoring period: from May 2022 (the beginning of monitoring) to July 2022, from October 2022 to July 2023, from October 2023 to July 2024, and from October 2024 to March 2025 (the end of the monitoring in this study). These periods corresponded to frequent seismic activity, as reflected in the higher density of green dots along the horizontal axis and their indication of elevated seismic energy densities on the vertical axis. During these periods, the raw hydrogen concentrations (blue bars in Figure 6a) consistently exceeded the anomaly threshold of 2.98 ppm. Notably, three seismic quiescence intervals were observed between the four active periods, typically occurring in August–September each year. During these relatively quiet periods, there was a marked decrease in seismic events.

To better visualize the segmented characteristics, Figure 6 is divided into subplots, as shown in Figure 7: Figure 7b,c represent two complete periods, including both seismic quiescence and seismic activity intervals, from August 1, 2022 to July 31, 2023 and from August 1, 2023 to July 31, 2024. Figure 7a,d present data from before July 31, 2022 and after August 1, 2024. To make the x-axis time lengths of these two segments comparable to those in Figure 7b,c, the horizontal axes were extended to August 1, 2021 and July 31, 2025, respectively, with empty observation values. A vertical comparison of Figure 7a–d shows that (1) during June–July, seismic activity was weak, and H_2 continued to be released at low concentrations; (2) during August–September, seismic activity was low, but short-term (approximately 15 days), high-intensity H_2 release was observed during seismic quiescence periods, a phenomenon seen in two of the three segments (Figure 7b,d); and (3) from October to May, seismic activity was intense, and H_2 release was strong, especially during January–March, further amplified by special seismic events (discussed in the next section).

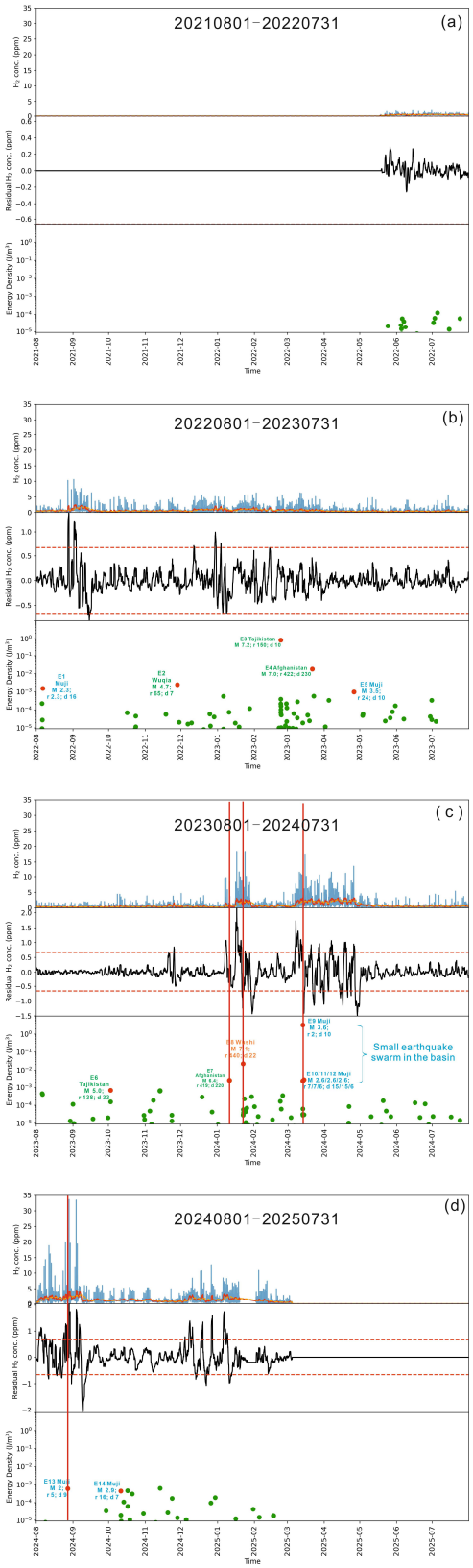

Figure 7. Segmented plots of Figure 6, with time intervals indicated in panels (**a**–**d**). Red points represent earthquakes within the Dobrovolsky preparation zone. Red vertical lines indicate the timing of individual seismic events, enabling comparison with H_2 concentration changes. Each red point is labeled with earthquake ID (e.g., E1–E14, as listed in Table S1), along with epicenter location, magnitude (*Ms*), distance to the observation spring (r, km), and focal depth (d, km). Label colors indicate earthquake locations: blue for events within the Muji Basin, yellow for those east of the observation site, and green for those to the west. Other symbols and legends are consistent with those in Figure 6.

The August–September anomalies can be interpreted as the result of two contributing factors. First, from July to September, elevated air and water temperatures reduce the solubility of H_2 in water, as described by Henry's law, thereby enhancing degassing in summer. Second, during tectonically inactive periods, dissolved gases may gradually accumulate in the spring system and then be released in short bursts. This process could be influenced by geological heterogeneity, particularly the anisotropy and uneven permeability of faults and aquifers. Such irregular hydrogeological conditions allow for ascending gases to accumulate locally during groundwater migration and then be abruptly released once a threshold is reached or triggered by minor tectonic motion. By contrast, during July–October 2023 (Figure 7c), although the frequency of large earthquakes was low, sustained low-magnitude seismic activity occurred, with energy densities consistently below 10^{-3} J/m^3. During this period, H2 concentrations remained stable and showed that no anomalous increases, suggesting that continuous low-energy seismic vibrations facilitated a steady, diffuse release of hydrogen, thereby preventing localized accumulation in the subsurface.

We recognize that the periodic features of H_2 release identified here and their correlation with seismic activity need further verification through the analysis of longer-term observation data. What is certain, however, is that H_2 release occurs during seismic periods of high activity, and strong H_2 release may also occur during relatively quiet seismic periods, indicating that H_2 release is not just a pre-seismic or post-seismic response. Rather, H_2 anomalies indicate periods of crustal tectonic instability. In other words, the sustained release of H_2 signals ongoing crustal activity, which seems to exhibit some regularity, though tectonic activity does not always lead to specific seismic events. This is understandable, as crustal activity is continuous, accompanied by ongoing geological gas release, but it does not necessarily generate earthquakes. This phenomenon suggested a stress-driven mechanism for hydrogen release, emphasizing the role of H_2 anomalies as indicators of fault-zone instability.

5.2.3. Response of H_2 Concentration Anomalies to Seismic Events

The initial motivation of this study was to identify pre-seismic and post-seismic responses in the H_2 time series, and more importantly, potential earthquake precursors. However, as shown in the seismic energy density scatter plot (Figure 6), the high frequency of earthquakes, the variability in energy densities affecting the observation site, and the frequent temporal overlaps among events complicate the identification of such relationships under current conditions. Nevertheless, the formula proposed by Dobrovolsky [52] was specifically developed to select earthquakes capable of exerting pre-seismic influences on monitoring stations. A notable feature of Figure 7 is that the earthquakes identified using the Dobrovolsky criterion (red dots) exhibit relatively high energy densities compared with other events (green dots) affecting the observation site. Accordingly, in this section, we focus on the pre-seismic responses of 14 earthquakes selected by this method. For clarity, these 14 events are categorized into three spatial groups according to their locations relative to the observation site, as indicated by color-coded labels in Figure 7: events within the Muji Basin (blue), to the east (yellow), and to the west (green).

A detailed analysis of the segmented datasets in Figure 7 indicates that most of the selected earthquakes did not display ideal precursor anomalies. Only E7, E8, the E9–E12 cluster, and E13 exhibited distinct pre-seismic H_2 anomalies, where both raw and residual H_2 concentrations exceeded the anomaly threshold. Among these, the precursor anomaly before E8 was particularly clear, suggesting a strong structural connection between the E8 seismogenic fault and the observation site. The E9–E12 cluster, which occurred within the Muji Basin, coincided with a pronounced H_2 anomaly (>2.98 ppm) that began seven days prior to E9 and persisted for nearly one month (Table S1). Such a seismic swarm

reflects intensified tectonic activity or accumulated seismic energy within the basin, which inevitably triggered strong degassing from the associated fault structures. By contrast, the pre-seismic anomalies associated with E7 and E13 are less conclusive. Specifically, E7 was an earthquake in Afghanistan, with an energy density on the order of 10^{-3} J/m^3. In comparison, E4, located very close to E7 (Figure 1), had a higher energy density of about 10^{-2} J/m^3 but did not show a notable precursor anomaly. This suggests that the observation site is relatively insensitive to earthquakes from the E4 source region. The apparent anomaly before E7 is more likely attributable to the periodic increase in the tectonic activity intensity discussed in Section 5.2.2, as elevated H_2 concentrations are observed around the E7 time window in Figure 7b,c,d. A similar interpretation applies to E13, which occurred within the Muji Basin in late August 2024. During the entire monitoring period, several earthquakes with magnitudes comparable to E13, and in some cases with even higher seismic energy densities at the observation site (e.g., E1, E5, E14), did not show obvious precursor anomalies. Considering that late August corresponds to a seismically quiescent period, but a strong H_2 anomaly unrelated to seismicity was also recorded in late August 2022, it is reasonable to infer that the pre-seismic anomaly observed before E13 was likewise the result of the periodic intensification of tectonic activity rather than a simple earthquake precursor. Nevertheless, the anomaly during E13 was the strongest of the entire monitoring period, indicating that the earthquake itself amplified the intensity of degassing that was already underway.

Spatial comparisons of seismic events provide additional insights. For instance, the E8 Wushi earthquake, located east of the observation site, had a lower energy density and a deeper focal depth (22 km) than the E3 Tajikistan earthquake to the west (10 km depth), yet it was associated with a stronger pre-seismic H_2 anomaly. This suggests that the seismogenic fault of E8 is more directly connected to the Muji Fault system, while E3 likely originated from a fault with weaker connectivity. This interpretation aligns with the results from multidisciplinary studies, including active fault mapping, GPS velocity field analysis, and focal mechanism solutions, which indicate that the present-day Pamir region is characterized by strong compression and shortening along its northern and western margins, while central–western Pamir is being tectonically separated from eastern Pamir along the nearly north–south-trending Kongur Extensional System (Figure 1) [43,44].

Post-seismic anomalies are also clearly observed following E8, the E9–E12 cluster, and E13. This is consistent with the interpretation above: the close tectonic association between the E8 source fault and the observation site likely prolonged its post-seismic modulation effect; the E9–E12 cluster within the Muji Basin induced a sustained release of geologic gases; and the anomaly after E13 corresponded to the highest H_2 concentration of the entire monitoring period, representing a post-quiescence, earthquake-triggered degassing event. It is also worth noting that, before interpreting the H_2 peak associated with E13, we ruled out instrumental errors or other external factors for the following reasons: As discussed in Section 5.1 and illustrated by the diurnal cycle in Figure 4a, daily H_2 concentrations followed a consistent rhythm, with maxima occurring between 17:00 and 18:00. The fact that the highest value coincided with the E13 event but still fit the regular diurnal pattern strongly supports the conclusion that the anomaly was caused by natural degassing rather than instrumental malfunction or anthropogenic interference.

6. Conclusions

This study reveals that hydrogen gas anomalies, although not consistent earthquake precursors, are useful indicators of broader crustal instability and fault-zone behavior. These results underscore the potential of continuous H_2 concentration monitoring as a valuable supplement to other geophysical methods in earthquake hazard assessment.

At the same time, the observations demonstrate the complexity of H_2 variability, which can be influenced by both environmental factors and subsurface processes such as gas accumulation and sudden release under heterogeneous hydrogeological conditions. A more thorough analysis on the basis of extended observation periods is required to better constrain these mechanisms and identify long-term patterns of H_2 release. Sustained monitoring is therefore essential, not only for deepening our understanding of the processes linking tectonic stress and fluid geochemistry but also for advancing the development of more reliable indicators for earthquake monitoring and prediction.

Supplementary Materials: The following supporting information can be downloaded at: https://www.mdpi.com/article/10.3390/app15179736/s1, Figure S1: Daily rainfall data from meteorological observation stations; Figure S2: Pearson correlation matrix of H_2 concentrations and meteorological parameters, where WT, AT, and AP are consistent with Table 1, and PP represents precipitation; Figure S3: Schematic diagram of the frequency distribution and cumulative proportion of H_2 concentration; Table S1: Observation data, precipitation data and earthquake catalog. Table S1 is an Excel file containing multiple sheets with the following data: (a) the original field-measured data for H_2 concentration, water temperature, air temperature, and atmospheric pressure; (2) the interpolated complete dataset for the above parameters; (3) daily precipitation records; (4) the earthquake catalog selected using the Dobrovolsky method; and (5) the earthquake catalog selected using seismic energy density.

Author Contributions: Conceptualization, J.T., J.L., Y.W. and M.H.; methodology, J.T. and X.Z.; software, S.C., B.Y. and Z.Z.; validation, B.Y. and Z.Z.; formal analysis, J.T., J.D., C.J. and C.L.; investigation, J.T., J.L. and Y.W.; data curation, J.T., M.H. and C.J.; writing—original draft preparation, J.T.; writing—review and editing, X.Z. and C.L.; supervision, X.Z.; funding acquisition, J.T. All authors have read and agreed to the published version of the manuscript.

Funding: This work was funded by the Institution Basal Research Fund of the Institute of Earthquake Forecasting, China Earthquake Administration (CEAIEF20240210), the Deep-land National Science and Technology Major Project (2024ZD100050305), Seismic Situation Tracking Project of the China Earthquake Administration (CEA-ZQGZ-202501074), and IGCP Project 724.

Institutional Review Board Statement: Not applicable.

Informed Consent Statement: Not applicable.

Data Availability Statement: The raw data supporting the conclusions of this article will be made available by the authors without reservation.

Conflicts of Interest: The authors declare no conflicts of interest.

References

1. Kennedy, D.; Norman, C. What don't we know? *Science* **2005**, *309*, 75. [CrossRef] [PubMed]
2. Beroza, G.; Segou, M.; Mostafa, S.M. Machine learning and earthquake forecasting—Next steps. *Nat. Commun.* **2021**, *12*, 4761. [CrossRef] [PubMed]
3. Wikelski, M.; Mueller, U.; Scocco, P.; Catorci, A.; Desinov, L.V.; Belyaev, M.Y.; Keim, D.; Pohlmeier, W.; Fechteler, G.; Martin, M.P. Potential short-term earthquake forecasting by farm animal monitoring. *Ethology* **2020**, *126*, 931–941. [CrossRef]
4. Claesson, L.; Skelton, A.; Graham, C.; Dietl, C.; Mörth, M.; Torssander, P.; Kockum, I. Hydrogeochemical changes before and after a major earthquake. *Geology* **2004**, *32*, 641–644. [CrossRef]
5. Takahashi, K.; Tsuji, T.; Ikeda, T.; Nimiya, H.; Nagata, Y.; Suemoto, Y. Underground structures associated with horizontal sliding at Uchinomaki hot springs, Kyushu, Japan, during the 2016 Kumamoto earthquake. *Earth Planets Space* **2019**, *71*, 87. [CrossRef]
6. Doglioni, C.; Barba, S.; Carminati, E.; Riguzzi, F. Fault on–off versus coseismic fluids reaction. *Geosci. Front.* **2014**, *5*, 767–780. [CrossRef]

7. Smeraglia, L.; Berra, F.; Billi, A.; Boschi, C.; Carminati, E.; Doglioni, C. Origin and role of fluids involved in the seismic cycle of extensional faults in carbonate rocks. *Earth Planet. Sci. Lett.* **2016**, *450*, 292–305. [CrossRef]
8. Hosono, T.; Masaki, Y. Post-seismic hydrochemical changes in regional groundwater flow systems in response to the 2016 Mw 7.0 Kumamoto earthquake. *J. Hydrol.* **2020**, *580*, 124340. [CrossRef]
9. Hosono, T.; Yamada, C.; Manga, M.; Wang, C.Y.; Tanimizu, M. Stable isotopes show that earthquakes enhance permeability and release water from mountains. *Nat. Commun.* **2020**, *11*, 2776. [CrossRef]
10. Siino, M.; Scudero, S.; Cannelli, V.; Piersanti, A.; D'Alessandro, A. Multiple seasonality in soil radon time series. *Sci. Rep.* **2019**, *9*, 8610. [CrossRef]
11. Raleigh, B. Prediction of Haicheng earthquake. *Eos Trans. AGU* **1977**, *58*, 236–272.
12. Skelton, A.; Andrén, M.; Kristmannsdóttir, H.; Stockmann, G.; Mrth, C.M.; Sveinbjrnsdóttir, R.; Jónsson, S.; Sturkell, E.; Gurúnardóttir, H.R.; Hjartarson, H. Changes in groundwater chemistry before two consecutive earthquakes in Iceland. *Nat. Geosci.* **2014**, *7*, 752–756. [CrossRef]
13. Woith, H.; Wang, R.; Maiwald, U.; Pekdeger, A.; Zschau, J. On the origin of geochemical anomalies in groundwaters induced by the Adana 1998 earthquake. *Chem. Geol.* **2013**, *339*, 177–186. [CrossRef]
14. Hashemi, S.M.; Negarestani, A.; Namvaran, M.; Musavi Nasab, S. An analytical algorithm for designing radon monitoring network to predict the location and magnitude of earthquakes. *J. Radioanal. Nucl. Chem.* **2013**, *295*, 2249–2262. [CrossRef]
15. Sahoo, S.K.; Katlamudi, M.; Barman, C.; Lakshmi, G.U. Identification of earthquake precursors in soil radon-222 data of Kutch, Gujarat, India using empirical mode decomposition based Hilbert Huang Transform. *J. Environ. Radioact.* **2020**, *222*, 106353. [CrossRef]
16. Sciarra, A.; Cantucci, B.; Coltorti, M. Learning from soil gas change and isotopic signatures during 2012 Emilia seismic sequence. *Sci. Rep.* **2017**, *7*, 14187. [CrossRef]
17. Zhang, L.; Liu, Y.; Guo, L.; Yang, D.; Fang, Z.; Chen, T.; Ren, H.; Yu, B. Isotope geochemistry of mercury and its relation to earthquake in the Wenchuan Earthquake Fault Scientific Drilling Project Hole-1 (WFSD-1). *Tectonophysics* **2014**, *619*, 79–85. [CrossRef]
18. Tian, J.; Zhou, X.; Yan, Y.; He, M.; Li, J.; Dong, J.; Liu, F.; Ouyang, S.; Li, Y.; Tian, L. Earthquake-induced impulsive release of water in the fractured aquifer system: Insights from the long-term hydrochemical monitoring of hot springs in the Southeast Tibetan Plateau. *Appl. Geochem.* **2023**, *148*, 105553. [CrossRef]
19. Wang, Y.; Zhou, X.; Tian, J.; Zhou, J.; He, M.; Li, J.; Dong, J.; Yan, Y.; Liu, F.; Yao, B. Volatile characteristics and fluxes of He-CO_2 systematics in the southeastern Tibetan Plateau: Constraints on regional seismic activities. *J. Hydrol.* **2023**, *617*, 129042. [CrossRef]
20. Yan, Y.; Zhou, X.; Liao, L.; Tian, J.; Li, Y.; Shi, Z.; Liu, F.; Ouyang, S. Hydrogeochemical characteristic of geothermal water and precursory anomalies along the Xianshuihe Fault Zone, Southwestern China. *Water* **2022**, *14*, 550. [CrossRef]
21. Chaudhuri, H.; Bari, W.; Iqbal, N.; Bhandari, R.K.; Ghose, D.; Sen, P.; Sinha, B. Long range gas-geochemical anomalies of a remote earthquake recorded simultaneously at distant monitoring stations in India. *Geochem. J.* **2011**, *45*, 137–156. [CrossRef]
22. Horiguchi, K.; Shimo, Y.; Matsuda, J.I. The $^3He/^4He$ ratios in hot spring gases after the Iwate-Miyagi Nairiku earthquake in 2008. *Geochim. Cosmochim. Acta Suppl.* **2009**, *73*, A550. [CrossRef]
23. Tian, J.; Zhou, X.; Liao, M.; He, M.; Zeng, Z.; Yan, Y.; Yao, B.; Wang, Y.; Cui, S.; Xing, G. Tectonic variations in NS-trending rifts, southern Tibetan Plateau: Insights from hydrothermal emissions and seismic activities. *J. Asian Earth Sci.* **2025**, *287*, 106599. [CrossRef]
24. Sugisaki, R. Geochemical features of gases and rocks along active faults. *Geochem. J.* **1980**, *14*, 101–112. [CrossRef]
25. Sugisaki, R.; Ido, M.; Takeda, H.; Isobe, Y.; Hayashi, Y.; Nakamura, N.; Satake, H.; Mizutani, Y. Origin of Hydrogen and Carbon Dioxide in Fault Gases and Its Relation to Fault Activity. *J. Geol.* **1983**, *91*, 239–258. [CrossRef]
26. Wakita, H.; Nakamura, Y.; Kita, I.; Fujii, N.; Notsu, K. Hydrogen release: New indicator of fault activity. *Science* **1980**, *210*, 188–190. [CrossRef] [PubMed]
27. Kita, I.; Matsuo, S.; Wakita, H. H_2 generation by reaction between H_2O and crushed rock: An experimental study on H_2 degassing from the active fault zone. *J. Geophys. Res. Solid Earth* **1982**, *87*, 10789–10795. [CrossRef]
28. Freund, F.T.; Freund, M.M. Paradox of peroxy defects and positive holes in rocks. Part I: Effect of temperature. *J. Asian Earth Sci.* **2015**, *114*, 373–383. [CrossRef]
29. Dogan, T.; Mori, T.; Tsunomori, F.; Notsu, K.J.P.; Geophysics, A. Soil H_2 and CO_2 Surveys at Several Active Faults in Japan. In *Terrestrial Fluids, Earthquakes and Volcanoes: The Hiroshi Wakita Volume II*; Pageoph Topical Volumes; Pérez, N.M., Gurrieri, S., King, C.-Y., Taran, Y., Eds.; Springer Science & Business Media: Berlin/Heidelberg, Germany, 2007; Volume 164, pp. 2449–2463.
30. Hirose, T.; Kawagucci, S.; Suzuki, K. Mechanoradical H_2 generation during simulated faulting: Implications for an earthquake-driven subsurface biosphere. *Geophys. Res. Lett.* **2011**, *38*, 245–255. [CrossRef]
31. Sato, M.; Sutton, A.; McGee, K. Anomalous hydrogen emissions from the San Andreas fault observed at the Cienega Winery, Central California. *Pure Appl. Geophys.* **1984**, *122*, 376–391. [CrossRef]

32. Zhou, X.; Du, J.; Chen, Z.; Cheng, J.; Li, Y. Geochemistry of soil gas in the seismic fault zone produced by the Wenchuan Ms 8.0 earthquake, southwestern China. *Geochem. Trans.* **2010**, *11*, 5. [CrossRef]
33. Mcgee, K.A.; Casadevall, T.J.; Sato, M.; Sutton, A.J.; Clark, M.D. *Hydrogen gas monitoring at Long Valley Caldera, California*; Open-File Report 82–930; United States Department of the Interior Geological Survey: Reston, VA, USA, 1982. [CrossRef]
34. Zhou, X.; Yan, Y.; Fang, W.; Wang, W.; Shi, H.; Li, P. Short-Term Seismic Precursor Anomalies of Hydrogen Concentration in Luojishan Hot Spring Bubbling Gas, Eastern Tibetan Plateau. *Front. Earth Sci.* **2021**, *8*, 586279. [CrossRef]
35. Mechie, J.; Yuan, X.; Schurr, B.; Schneider, F.; Sippl, C.; Ratschbacher, L.; Minaev, V.; Gadoev, M.; Oimahmadov, I.; Abdybachaev, U.; et al. Crustal and uppermost mantle velocity structure along a profile across the Pamir and southern Tien Shan as derived from project TIPAGE wide-angle seismic data. *Geophys. J. Int.* **2012**, *188*, 385–407. [CrossRef]
36. Schwab, M.; Ratschbacher, L.; Siebel, W.; McWilliams, M.; Minaev, V.; Lutkov, V.; Chen, F.; Stanek, K.; Nelson, B.; Frisch, W.; et al. Assembly of the Pamirs: Age and origin of magmatic belts from the southern Tien Shan to the southern Pamirs and their relation to Tibet. *Tectonics* **2004**, *23*, TC4002. [CrossRef]
37. Yin, A.; Harrison, T.M. Geologic evolution of the Himalayan-Tibetan orogen. *Annu. Rev. Earth Planet. Sci.* **2000**, *28*, 211–280. [CrossRef]
38. Zubovich, A.V.; Wang, X.; Scherba, Y.G.; Schelochkov, G.G.; Reilinger, R.; Reigber, C.; Mosienko, O.I.; Molnar, P.; Michajljow, W.; Makarov, V.I. GPS velocity field for the Tien Shan and surrounding regions. *Tectonics* **2010**, *29*, TC6014. [CrossRef]
39. Robinson, A.C.; Yin, A.; Manning, C.E.; Harrison, T.M.; Zhang, S.H.; Wang, X.F. Tectonic evolution of the northeastern Pamir: Constraints from the northern portion of the Cenozoic Kongur Shan extensional system, western China. *Geol. Soc. Am. Bull.* **2004**, *116*, 953–973. [CrossRef]
40. Thiede, R.C.; Sobel, E.R.; Chen, J.; Schoenbohm, L.M.; Stockli, D.F.; Sudo, M.; Strecker, M.R. Late Cenozoic extension and crustal doming in the India-Eurasia collision zone: New thermochronologic constraints from the NE Chinese Pamir. *Tectonics* **2013**, *32*, 763–779. [CrossRef]
41. Chevalier, M.L.; Pan, J.; Li, H.; Liu, D.; Wang, M. Quantification of both normal and right-lateral late Quaternary activity along the Kongur Shan extensional system, Chinese Pamir. *Terra Nova* **2015**, *27*, 379–391. [CrossRef]
42. Li, T.; Schoenbohm, L.M.; Chen, J.; Yuan, Z.; Feng, W.; Li, W.; Xu, J.; Owen, L.A.; Sobel, E.R.; Zhang, B.; et al. Cumulative and Coseismic (During the 2016 Mw 6.6 Aketao Earthquake) Deformation of the Dextral-Slip Muji Fault, Northeastern Pamir Orogen. *Tectonics* **2019**, *38*, 3975–3989. [CrossRef]
43. Deng, J.; Han, F.; Li, T.; Zhang, B.; Xu, J.; Yao, Y. Late-Quaternary slip sense and rate of the Muji fault, northeastern Pamir. *Quat. Sci.* **2020**, *40*, 114–123.
44. Chen, J.; Li, T.; Sun, J.; Fang, L.; Yao, Y.; Li, Y.; Wang, H.; Fu, B. Coseismic surface ruptures and seismogenic Muji fault of the 25 November 2016 Arketao Mw 6.6 earthquake in northern Pamir. *Seismol. Geol.* **2016**, *38*, 1160–1174.
45. Yang, H.; Wu, X.; Cui, H.; Wang, W.; Cheng, Y.; Gong, X.; Luo, X.; Lin, Q. Formation Mechanism of Muji Travertine in the Pamirs Plateau, China. *Minerals* **2024**, *14*, 1192. [CrossRef]
46. Chen, Z.; Song, X.; Sun, M.; Yu, H.; Guo, X.; Yin, X.; Song, Q. Microstructure, geochemical and genesis of coated grains in the Muji Basin, Xinjiang. *Quat. Sci.* **2023**, *43*, 173–186.
47. Dudek, G. STD: A Seasonal-Trend-Dispersion Decomposition of Time Series. *IEEE Trans. Knowl. Data Eng.* **2023**, *35*, 10339–10350. [CrossRef]
48. Quan, J.; Zhan, W.; Chen, Y.; Wang, M.; Wang, J. Time series decomposition of remotely sensed land surface temperature and investigation of trends and seasonal variations in surface urban heat islands. *J. Geophys. Res. Atmos.* **2016**, *121*, 2638–2657. [CrossRef]
49. Freund, F. Pre-earthquake signals: Underlying physical processes. *J. Asian Earth Sci.* **2011**, *41*, 383–400. [CrossRef]
50. Rundle, J.B.; Turcotte, D.L.; Shcherbakov, R.; Klein, W.; Sammis, C. Statistical physics approach to understanding the multiscale dynamics of earthquake fault systems. *Rev. Geophys.* **2003**, *41*, 1019. [CrossRef]
51. Dobrovolsky, I.; Zubkov, S.; Miachkin, V. Estimation of the size of earthquake preparation zones. *Pure Appl. Geophys.* **1979**, *117*, 1025–1044. [CrossRef]
52. Wang, C.Y. Liquefaction beyond the near field. *Seismol. Res. Lett.* **2007**, *78*, 512–517. [CrossRef]
53. Kautz, C.H.; Heron, P.R.; Loverude, M.E.; McDermott, L.C. Student understanding of the ideal gas law, Part I: A macroscopic perspective. *Am. J. Phys.* **2005**, *73*, 1055–1063. [CrossRef]
54. Henry, W. III. Experiments on the quantity of gases absorbed by water, at different temperatures, and under different pressures. *Philos. Trans. R. Soc. Lond.* **1803**, *93*, 29–274. [CrossRef]
55. Hannan, E.J. *Multiple Time Series*; John Wiley & Sons: New York, NY, USA, 1970.
56. Ambrosino, F.; Thinová, L.; Briestenský, M.; Šebela, S.; Sabbarese, C. Detecting time series anomalies using hybrid methods applied to Radon signals recorded in caves for possible correlation with earthquakes. *Acta Geod. Geophys.* **2020**, *55*, 405–420. [CrossRef]
57. Sahoo, S.K.; Katlamudi, M.; Gakka, U.L. Singular spectrum analysis on soil radon time series (222 Rn) in Kachchh, Gujarat, India: Detection of periodic oscillations and earthquake precursors. *Arab. J. Geosci.* **2020**, *13*, 973. [CrossRef]

58. Janik, M.; Bossew, P.; Kurihara, O. Machine learning methods as a tool to analyse incomplete or irregularly sampled radon time series data. *Sci. Total Environ.* **2018**, *630*, 1155–1167. [CrossRef] [PubMed]
59. Mir, A.A.; Çelebi, F.V.; Alsolai, H.; Qureshi, S.A.; Rafique, M.; Alzahrani, J.S.; Mahgoub, H.; Hamza, M.A. Anomalies Prediction in Radon Time Series for Earthquake Likelihood Using Machine Learning-Based Ensemble Model. *IEEE Access* **2022**, *10*, 37984–37999. [CrossRef]
60. Tareen, A.D.K.; Nadeem, M.S.A.; Kearfott, K.J.; Abbas, K.; Khawaja, M.A.; Rafique, M. Descriptive analysis and earthquake prediction using boxplot interpretation of soil radon time series data. *Appl. Radiati. Isot.* **2019**, *154*, 108861. [CrossRef] [PubMed]
61. Barkat, A.; Ali, A.; Hayat, U.; Crowley, Q.G.; Rehman, K.; Siddique, N.; Haidar, T.; Iqbal, T. Time series analysis of soil radon in Northern Pakistan: Implications for earthquake forecasting. *Appl. Geochem.* **2018**, *97*, 197–208. [CrossRef]
62. Fu, C.C.; Walia, V.; Yang, T.F.; Lee, L.C.; Liu, T.K.; Chen, C.H.; Kumar, A.; Lin, S.J.; Lai, T.H.; Wen, K.L. Preseismic anomalies in soil-gas radon associated with 2016 M 6.6 Meinong earthquake, Southern Taiwan. *Terr. Atmos. Ocean. Sci.* **2017**, *28*, 787–798. [CrossRef]
63. Külahcı, F.; Çiçek, Ş. Time-series analysis of water and soil radon anomalies to identify micro–macro-earthquakes. *Arab. J. Geosci.* **2015**, *8*, 5239–5246. [CrossRef]
64. Ambrosino, F.; Pugliese, M.; Roca, V.; Sabbarese, C. Innovative methodologies for the analysis of radon time series. *Nuovo C. C* **2018**, *41*, 223–228.
65. Barman, C.; Ghose, D.; Sinha, B.; Deb, A. Detection of earthquake induced radon precursors by Hilbert Huang Transform. *J. Appl. Geophys.* **2016**, *133*, 123–131. [CrossRef]
66. Yang, T.; Fu, C.C.; Walia, V.; Chen, C.H.; Chyi, L.; Liu, T.K.; Song, S.R.; Lee, M.; Lin, C.W.; Lin, C.C. Seismo-geochemical variations in SW Taiwan: Multi-parameter automatic gas monitoring results, Terrestrial Fluids, Earthquakes and Volcanoes. *Pure Appl. Geophys.* **2006**, *163*, 693–709. [CrossRef]
67. Soldati, G.; Cannelli, V.; Piersanti, A. Monitoring soil radon during the 2016–2017 central Italy sequence in light of seismicity. *Sci. Rep.* **2020**, *10*, 13137. [CrossRef] [PubMed]
68. Fu, C.C.; Yang, T.F.; Chen, C.H.; Lee, L.C.; Wu, Y.M.; Liu, T.K.; Walia, V.; Kumar, A.; Lai, T.H. Spatial and temporal anomalies of soil gas in northern Taiwan and its tectonic and seismic implications. *J. Asian Earth Sci.* **2017**, *149*, 64–77. [CrossRef]
69. Hartmann, J.; Levy, J.K. Hydrogeological and Gasgeochemical Earthquake Precursors—A Review for Application. *Nat. Hazards* **2005**, *34*, 279–304. [CrossRef]
70. Barbieri, M.; Franchini, S.; Barberio, M.D.; Billi, A.; Boschetti, T.; Giansante, L.; Gori, F.; Jónsson, S.; Petitta, M.; Skelton, A. Changes in groundwater trace element concentrations before seismic and volcanic activities in Iceland during 2010–2018. *Sci. Total Environ.* **2021**, *793*, 148635. [CrossRef]
71. Barberio, M.D.; Gori, F.; Barbieri, M.; Billi, A.; Caracausi, A.; De Luca, G.; Franchini, S.; Petitta, M.; Doglioni, C. New observations in Central Italy of groundwater responses to the worldwide seismicity. *Sci. Rep.* **2020**, *10*, 17850. [CrossRef]
72. Franchini, S.; Agostini, S.; Barberio, M.D.; Barbieri, M.; Billi, A.; Boschetti, T.; Pennisi, M.; Petitta, M. HydroQuakes, central Apennines, Italy: Towards a hydrogeochemical monitoring network for seismic precursors and the hydro-seismo-sensitivity of boron. *J. Hydrol.* **2021**, *598*, 125754. [CrossRef]
73. Li, B.; Shi, Z.; Wang, G.; Liu, C. Earthquake-related hydrochemical changes in thermal springs in the Xianshuihe Fault zone, Western China. *J. Hydrol.* **2019**, *579*, 124175. [CrossRef]
74. Onda, S.; Sano, Y.; Takahata, N.; Kagoshima, T.; Miyajima, T.; Shibata, T.; Pinti, D.L.; Lan, T.; Kim, N.K.; Kusakabe, M. Groundwater oxygen isotope anomaly before the M6. 6 Tottori earthquake in Southwest Japan. *Sci. Rep.* **2018**, *8*, 4800. [CrossRef] [PubMed]
75. Shi, Z.; Wang, G.; Manga, M.; Wang, C.Y. Mechanism of co-seismic water level change following four great earthquakes–insights from co-seismic responses throughout the Chinese mainland. Earth Planet. *Sci. Lett.* **2015**, *430*, 66–74. [CrossRef]